The Estimation of Convective Mass Flux from Radar Reflectivities

VICKAL V. KUMAR,[*,+,++] ALAIN PROTAT,[#] CHRISTIAN JAKOB,[*,+] CHRISTOPHER R. WILLIAMS,[@,&] SURENDRA RAUNIYAR,[#] GRAEME L. STEPHENS,[**] AND PETER T. MAY[#]

[*] *School of Earth, Atmosphere and Environment, Monash University, Melbourne, Victoria, Australia*
[+] *ARC Centre of Excellence for Climate System Science, Monash University, Melbourne, Victoria, Australia*
[#] *Centre for Australian Weather and Climate Research, Bureau of Meteorology–CSIRO, Melbourne, Victoria, Australia*
[@] *University of Colorado, Boulder, Colorado*
[&] *Physical Sciences Division, NOAA/Earth System Research Laboratory, Boulder, Colorado*
[**] *Department of Atmospheric Science, Colorado State University, Fort Collins, Colorado*

(Manuscript received 14 July 2015, in final form 18 January 2016)

ABSTRACT

Cumulus parameterizations in general circulation models (GCMs) frequently apply mass-flux schemes in their description of tropical convection. Mass flux constitutes the product of the fractional area covered by cumulus clouds in a model grid box and the vertical velocity within the cumulus clouds. The cumulus area fraction profiles can be derived from precipitating radar reflectivity volumes. However, the vertical velocities are difficult to observe, making the evaluation of mass-flux schemes difficult. In this paper, the authors develop and evaluate a parameterization of vertical velocity in convective (cumulus) clouds using only radar reflectivities collected by a C-band polarimetric research radar (CPOL), operating at Darwin, Australia. The parameterization is trained using vertical velocity retrievals from a dual-frequency wind profiler pair located within the field of view of CPOL. The parametric model uses two inputs derived from CPOL reflectivities: the 0-dBZ echo-top height (0-dBZ ETH) and a height-weighted column reflectivity index (Z_{HWT}). The 0-dBZ ETH determines the shape of the vertical velocity profile, while Z_{HWT} determines its strength. The evaluation of these parameterized vertical velocities using (i) the training dataset, (ii) an independent wind-profiler-based dataset, and (iii) 1 month of dual-Doppler vertical velocity retrievals indicates that the statistical representation of vertical velocity is reasonably accurate up to the 75th percentile. However, the parametric model underestimates the extreme velocities. The method allows for the derivation of cumulus mass flux and its variability on current GCM scales based only on reflectivities from precipitating radar, which could be valuable to modelers.

1. Introduction

General circulation models (GCMs) commonly use a cumulus mass-flux scheme to simulate tropical convection (Arakawa 2004; Wu 2012). From a GCM perspective, cumulus mass flux is the product of air density, fractional area covered by convection in the model grid box (denoted as convective area fraction), and vertical velocity in convective clouds. The convective area fractions can be accurately estimated by ground-based and spaceborne precipitation radars (e.g., TRMM, GPM, and *CloudSat*) using convective–stratiform partitioning techniques (e.g., Steiner et al. 1995). However, it is much more challenging to estimate vertical velocities. This has hindered the development and evaluation of mass-flux schemes using observations. In this paper, we develop and evaluate a new vertical velocity retrieval technique to determine cumulus mass flux on a scale of 100 km at a tropical location, Darwin, Australia.

Many attempts have been made to characterize vertical velocity in convective clouds using a variety of instruments: aircraft in situ penetrations (e.g., Byers and Braham 1949; Marwitz 1973; LeMone and Zipser 1980; Anderson et al. 2005), airborne vertically pointing Doppler radars (e.g., Heymsfield et al. 2010), vertically pointing ground-based wind profilers (e.g., May and

[++] Current affiliation: Space Weather Services, Australian Bureau of Meteorology, Haymarket, New South Wales, Australia.

Corresponding author address: Vickal V. Kumar, Space Weather Services, Australian Bureau of Meteorology and CSIRO, P.O. Box 1386 Haymarket, NSW 1240, Australia.
E-mail: v.kumar@bom.gov.au

DOI: 10.1175/JAMC-D-15-0193.1

Rajopadhyaya 1999; Williams 2012; Giangrande et al. 2013; Kumar et al. 2015), dual-polarization radar (e.g., Ryzhkov et al. 2013), and scanning radars in single- or multiple-Doppler configurations (e.g., Laroche and Zawadzki 1994; Protat and Zawadzki 1999; Collis et al. 2013). To estimate mass flux from observations, we need long-term measurements of vertical velocity inside convective clouds at high horizontal and vertical resolutions. None of the aforementioned measurement techniques are thought to be ideal for this. Aircraft do not penetrate in all types of cores because of safety concerns and the sample size is limited in terms of geographical location and large-scale conditions, making it difficult to use these measurements statistically. Dual-frequency vertically pointing wind profiler observations provide accurate estimates of vertical velocity in convection and at high vertical resolution (Williams 2012; Kumar et al. 2015). However, they cannot sample the full GCM grid box. While vertical and horizontal wind vectors retrieved from one or more scanning Doppler radars capture the full 3D motions within all individual precipitating clouds over a volume equivalent to a GCM grid box (100 km × 100 km in the horizontal and 20 km in the vertical) or larger, this retrieval technique requires model constraints and assumptions that still need to be evaluated (e.g., Collis et al. 2013). Single-Doppler retrievals also require additional assumptions that by construction degrade the ''instantaneous'' quality of the three-dimensional wind retrieval (e.g., Laroche and Zawadzki 1994; Shapiro et al. 2003). The capacity of single-Doppler radars to approximate the statistical properties of vertical velocities is unknown.

The ability to quantitatively derive vertical velocity from radar reflectivities only would be invaluable, as such a technique could then be applied to all ground-based and spaceborne precipitation radar types, even those without Doppler and polarimetric capabilities. Zipser and Lutz (1994) and Luo et al. (2014) describe attempts to do this. Zipser and Lutz (1994) showed the potential of using vertical profiles of radar reflectivity (Z profiles) and vertical gradients in Z profiles (reflectivity lapse rates) as a proxy for vertical velocities in cumulus clouds, but did not propose a quantitative parametric representation to link vertical velocity and radar reflectivity gradients. In the Zipser and Lutz (1994) study, large negative reflectivity lapse rates above the freezing level corresponded to weaker updraft speeds. Luo et al. (2014) noted a similar relationship between vertical velocity and Z profiles in cumulus clouds using satellite observations. The vertical velocity estimates used in their study were derived from time-delayed infrared measurements from the Moderate Resolution Imaging Spectroradiometer (MODIS) on board *Aqua* and Imaging Infrared Radiometer (IIR) on board *CALIPSO* (Luo et al. 2014). Again, no parametric representation of vertical velocity as a function of time-differenced IR measurements was proposed. As will be discussed below, an obvious advantage of our study compared to these studies is that we will use reference vertical velocity measurements from a dual-frequency wind profiler pair (Williams 2012; Kumar et al. 2015) to quantitatively link convective vertical velocities and radar reflectivities.

Our focus is to provide a robust observational reference for tropical cumulus mass flux at scales relevant to current GCMs (100 km × 100 km) using a variety of measurement techniques. Kumar et al. (2015) used dual-frequency wind profiler observations to characterize the mean vertical profile of vertical velocity and mass flux and its variability as a function of the large-scale environmental conditions and convective cloud depth. It was shown that cumulus mass flux at typical current GCM resolutions is primarily regulated by the convective area fraction, which in the vertically pointing wind profiler case was estimated indirectly using a temporal aggregation technique. The magnitudes of the vertical velocity were found to play a secondary role. This suggests that a first-order estimate of vertical velocity could be sufficient to accurately estimate cumulus mass flux. Based on this idea, the aim of this paper is to estimate mass flux using single volumetric radar observations, taking advantage of the accurate convective area fractions provided by volumetric radars, and exploring the potential of using radar reflectivities to estimate vertical velocities.

The main task is to investigate whether indices derived from radar reflectivity contain sufficient information to quantitatively estimate the magnitude of vertical velocities in updraft and downdraft cores of individual convective clouds. A relationship between radar reflectivity and vertical velocity is somewhat expected, as discussed in Zipser and Lutz (1994) and Luo et al. (2014). To investigate the robustness of such a relationship, we combine a thoroughly tested database of vertical velocities extracted from a dual-frequency wind profiler pair (May and Rajopadhyaya 1999; Williams 2012; Kumar et al. 2015) with radar reflectivity from a C-band polarimetric research radar (CPOL; Keenan et al. 1998) around Darwin, Australia. Three wet seasons of data are included in this analysis. From the C-band radar reflectivities, a set of reflectivity indices is developed and correlated with the vertical velocities to assess which reflectivity indices can provide useful constraints to build a parametric representation of vertical velocity. The estimates from that relationship are then combined

with observations of fractional coverage with convection to provide mass-flux estimates.

The paper is organized as follows. In section 2, the datasets used in the study are introduced. Statistical relationships between the dual-frequency wind profiler retrievals of the vertical profile of vertical velocity (w profiles) and the CPOL vertical profile of radar reflectivity (Z profiles) are investigated in section 3a. A parametric model to convert Z profiles into w profiles is developed in section 3b. This is followed by an evaluation of derived vertical velocity from CPOL Z profiles against vertical velocity from wind profiler and dual-Doppler 3D wind retrievals in section 3c. The estimation of mass flux from CPOL reflectivities is discussed in section 4.

2. Data

In this study, we want to develop a radar tool to estimate w profiles in convective clouds using Z profiles from volumetric radar information. The inputs needed to develop our radar tool include collocated radar reflectivities and in-cloud vertical velocity estimates. To achieve this, we combine two wet seasons (October 2005–April 2006 and October 2006–April 2007) of a vertical velocity dataset from a pair of wind profilers with collocated reflectivities from the CPOL radar (Kumar et al. 2015). The profiler pair is located within the field of view of CPOL. As is common practice in statistical modeling we evaluate the radar tool with an independent dataset not used in its training. To do so we use another wet season (October 2009–April 2010) of wind profiler vertical velocity and a month (November 2005) of dual-Doppler vertical velocity retrievals. The CPOL and profiler datasets are described in more detail below. The dual-Doppler retrieval setup relevant to the Darwin site is explained briefly in section 3c(3), and more details are in Protat and Zawadzki (1999) and Collis et al. (2013).

a. Darwin CPOL radar

CPOL is predominantly sensitive to precipitation size particles of diameter exceeding 0.5 mm. In this study, we only use reflectivity profiles (or simply Z profiles) from the CPOL radar. These reflectivities have been corrected for attenuation using the dual-polarization method developed by Bringi et al. (2001). The reflectivities have been interpolated onto a cubic grid with a horizontal grid size of 2.5 km × 2.5 km and a vertical grid size of 0.5 km and are available in each grid box every 10 min (e.g., Kumar et al. 2013a). The convective area fraction over the radar domain is also estimated every 10 min (see Kumar et al. 2015) using the algorithm developed by Steiner et al. (1995). To minimize any issues that might occur during the interpolation of the radar data in the Cartesian grid, only data between the ranges of 20 and 120 km (44 000 km^2) and at heights greater than 2.5 km are analyzed. The same data limits were used elsewhere (e.g., Kumar et al. 2013a,b).

The CPOL spatial coverage is equivalent to about four 100-km GCM grid boxes. Even if we expect that the GCM grid resolution will increase to a finer scale in the future, the mean convective area fraction and w profiles discussed here would still be useful to modelers. Kumar et al. (2015) showed that the average convective area fraction profiles for different GCM grid resolution ranging from 10 to 100 km were remarkably similar in the vicinity of the wind profiler. However, the different grid resolutions do affect the variability in convective area fraction, with finer grid resolution naturally producing larger variability because of an increased incidence of both very large and very small area fractions. In contrast, changes to GCM grid size will not affect the w profiles since our approach to derive vertical velocities in convective clouds, as discussed below, uses the individual radar pixels.

Our objective is to estimate w profiles in convective clouds only. Convective–stratiform partitioning of the radar pixels is obtained by applying a convective pixel identification algorithm (Steiner et al. 1995) to the radar reflectivities at the 2.5-km height level. The whole vertical profile is then assigned the same classification as that at the 2.5-km level. However, reflectivities from cirrus anvils above the convective towers are filtered out. To do so we use the 0-dBZ echo-top height (0-dBZ ETH) extracted from the CPOL reflectivities. Specifically, the 0-dBZ ETH corresponds to the height where the reflectivity is the closest to 0 dBZ, but with a reflectivity value within the range from −5 to +5 dBZ, and provided there is a vertically continuous reflectivity between the lowest CPOL height level of 2.5 km and this 0-dBZ ETH. Previous studies have shown that the 0-dBZ ETH from C-band radar are usually within 1 km of cloud tops estimated by ground and spaceborne millimeter cloud radars (e.g., Casey et al. 2012; Kumar et al. 2013a). The 0-dBZ ETH is also used to separate the observed convective clouds as either congestus (0-dBZ ETH between 3 and 7 km), deep (7 and 15 km), or overshooting (>15 km; Kumar et al. 2013a, 2014), allowing us to contrast the vertical velocities associated with these different cumulus modes. It was shown by Kumar et al. (2013a) that 0-dBZ ETH can be used to objectively identify the different cumulus modes.

b. *The Darwin wind profiler radar pair*

The Darwin 50- and 920-MHz wind profiler pair is located 23.6 km southwest of CPOL (see Fig. 1 of May et al. 2002), and thereby provides direct observations of w profiles within a particular CPOL reflectivity column. A detailed description of the profiler vertical velocity retrieval technique can be found in Williams (2012) and Kumar et al. (2015). A brief summary is provided below.

The 50-MHz profiler spectra contain both the wanted signals of vertical velocity of air parcels and unwanted signal of contamination from hydrometeor fall velocity. The spectra from the 920-MHz profiler, on the other hand, are only sensitive to hydrometeor fall velocity, and therefore are used to filter the unwanted signals from the 50-MHz profiler spectra. The original profiler velocities are retrieved at a much finer resolution of 0.1 km in height and 1 min in time, and are then regridded in bins of 0.5 km in height and 10-min steps in time, to match the CPOL resolutions. The velocity profiles obtained with the regridded data are very similar to those found with data at the original resolution (see Kumar et al. 2015). No vertical velocities from heights below 2.5 km and greater than CPOL-determined 0-dBZ ETH over the profiler site or the set cutoff height of 14 km, whichever is less, are kept in the analysis. This ensures that the velocities are always from within clouds and within the altitude ranges of CPOL data. The 14 km cutoff was chosen as a compromise: not very high since the sensitivity of the profiler drops with height (May and Rajopadhyaya 1999), and not very low so that they are of value to modelers and comparable with observations from elsewhere (e.g., Heymsfield et al. 2010). Each 10-min profiler data block is flagged as either convective or stratiform using the classification of the corresponding CPOL pixel. There are a total of 246 10-min convective profiles occurring over the profiler site during the two wet seasons, and these are analyzed in detail in the next section. As the focus of this study is on convective clouds, observations from stratiform intervals have being discarded in the statistical analysis.

3. Results

a. *Characteristics of the wind profiler w-profile observations as function of Z-profile properties from CPOL*

In the following subsections, we explore the mean and variability characteristics of w profiles retrieved from the profiler as a function of various reflectivity indices derived from the CPOL data. The aim is to investigate which reflectivity indices can be used to estimate w profiles. Although many other radar products—such as Doppler wind (e.g., Shapiro et al. 2003), spectral width (Spoden et al. 2012), and cloud droplet size distribution (e.g., Lu et al. 2012)—are known to be affected by vertical velocities, these relationship are not investigated here because we want to develop a tool that can be useful to all radar types, even those without Doppler and polarimetric capabilities.

1) MEAN W PROFILES FOR THE DIFFERENT CUMULUS MODES

The 246 selected 10-min convective profiles are divided into three cumulus cloud modes based on the 0-dBZ ETH extracted from CPOL Z-profile data (e.g., Kumar et al. 2013a). There are 62 congestus, 132 deep, and 52 overshooting cells defined with 0-dBZ ETH ranges of 3–7 km (congestus), 7–15 km (deep), and >15 km (overshooting). A 10-min convective profile can contain both updraft ($w > 0\,\mathrm{m\,s^{-1}}$) and downdraft regions. Data from updraft and downdraft regions are analyzed separately throughout the paper. Figure 1a shows the mean w profiles using all updraft and downdraft data points, as well as separately for the three cumulus modes. The spread and number of profiler data points associated with each cumulus mode are shown in Figs. 1b and 1c, respectively.

The mean updraft vertical velocity associated with all 246 cells (solid curve in Fig. 1) increases gradually with height, with peak magnitude of $\sim 5\,\mathrm{m\,s^{-1}}$ at 12-km height. The mean updraft w profiles for different cumulus modes are markedly different. For the congestus mode (dotted curve), the average updraft magnitudes are the smallest and generally constant with height. The deep convective mode (dashed curve) shows a bimodal structure with a weak peak at 6 km and a stronger peak above 10-km height. In contrast, the overshooting mode (dotted–dashed curve) is characterized by the strongest mean updraft, which increases rapidly with increasing height. Several competing processes affect the updraft speeds in cumulus clouds (e.g., Zipser 2003; Fierro et al. 2009; Heymsfield et al. 2010). The acceleration in updraft speeds near the freezing level and at higher altitudes is likely due to positive buoyancy provided by latent heating from freezing of liquid drops and supercooled liquid drops, respectively. The updraft cores are also warmer and less dense compared to the colder and denser environment, further promoting buoyancy. The deceleration in updraft speeds at higher altitude can be attributed to the entrainment/detrainment processes, the drag effect caused by water loading and the negative buoyancy induced by in-cloud density temperature becoming lower than the environment ambient temperatures.

In contrast, the mean convective downdraft profile is characterized by a much weaker magnitude of $\sim 1\,\mathrm{m\,s^{-1}}$.

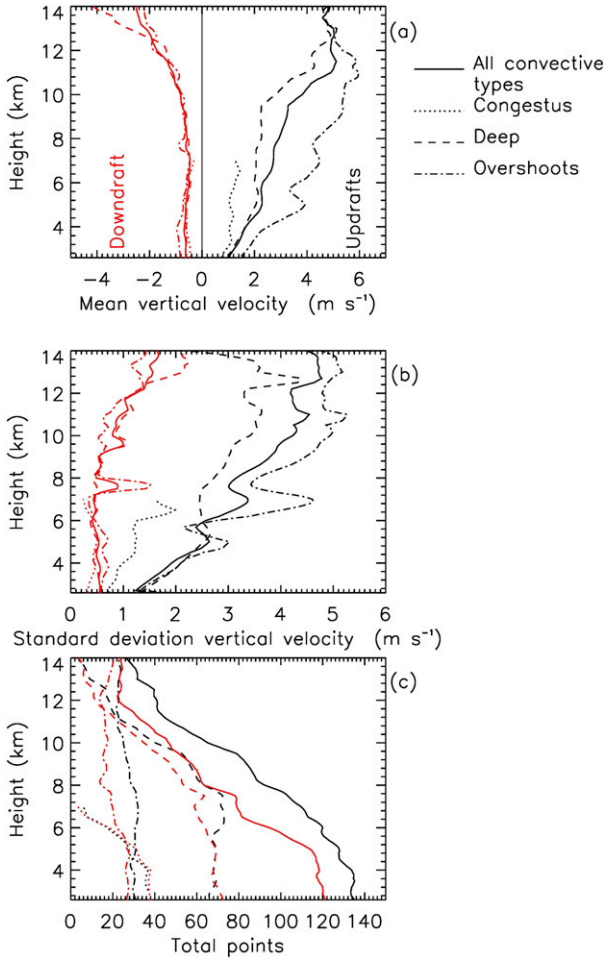

FIG. 1. Profiles of (a) mean updraft (black) and downdraft (red) vertical velocity associated with all 246 convective clouds (solid curve), 62 congestus = dotted curve), 132 deep (dashed curve), and 51 overshooting convection (dotted–dashed curve); (b) standard deviation of vertical velocities; (c) total number points used in the calculations.

A possible reason for weak downdrafts in convective profiles is because downdrafts typically occur close to or in stratiform regions, both ahead of and behind the convective core (e.g., Kumar et al. 2015), which have been removed from our analysis because our focus is convective mass flux. The downdraft speeds are almost constant throughout the cloud layer, with slightly larger values near the tops of very deep clouds and the weakest values in the midlevels. There is only a slight difference in mean downdraft profiles for the different cumulus modes. Downdrafts forming below the freezing level can be explained by negative buoyancy initiated by precipitation loading and enhanced by cooling because of the phase change of precipitation (e.g., Hjelmfelt et al. 1989; May and Rajopadhyaya 1999). Those forming in the upper levels are explained in Kumar et al. (2015) as

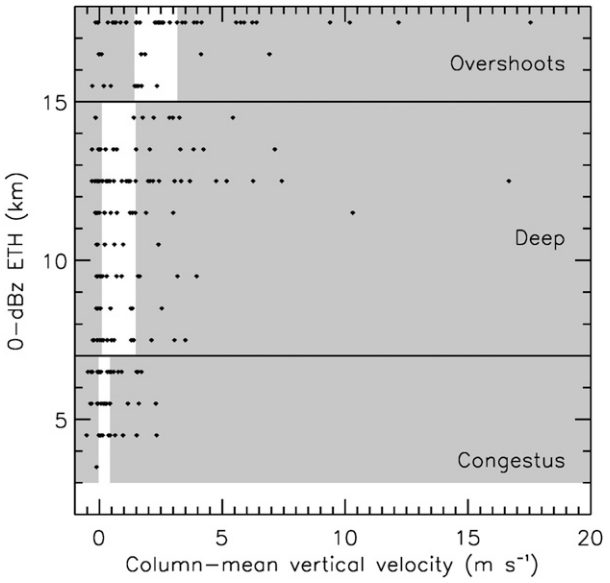

FIG. 2. Scatterplot of column-mean vertical velocity as a function of 0-dBZ echo-top height. It contains a total of 246 data points: one mean vertical velocity was calculated per cumulus cloud (a total of 246 cumulus columns) using the wind-profiler vertical velocities. The shaded regions in three cumulus categories represent the smallest one-third and the largest one-third of mean vertical velocities. These tercile boundaries are $w \le -0.04\ \mathrm{m\,s^{-1}}$ and $w \ge 0.44\ \mathrm{m\,s^{-1}}$ for congestus mode, $w \le 0.10\ \mathrm{m\,s^{-1}}$ and $w \ge 1.48\ \mathrm{m\,s^{-1}}$ for deep mode, and $w \le 1.42\ \mathrm{m\,s^{-1}}$ and $w \ge 3.18\ \mathrm{m\,s^{-1}}$ for overshooting mode.

initiated by convergence between air detrained from the tops of the updrafts and slower-moving ambient air.

The observed mean updraft and downdraft w profiles in cumulus clouds using the wind profiler observations are consistent with previous studies (May and Rajopadhyaya 1999; Heymsfield et al. 2010; Giangrande et al. 2013). In conclusion, the three 0-dBZ ETH classes, a proxy for cumulus modes, are likely useful for parameterization of w profiles because of well-marked differences in updraft profiles of the different cumulus modes.

2) VARIABILITY IN THE W PROFILES' MEASUREMENTS

Figure 2 shows a scatterplot of column-mean vertical velocity as a function of 0-dBZ ETH for all 246 convective profiles. Column-mean vertical velocities of the congestus mode are generally smaller than those of the deep convective mode, which are themselves generally smaller than those of the overshooting mode. However, the main result from Fig. 2 is that there is a very large variability in column-mean vertical velocity within each of these cumulus cloud modes. This result clearly shows that 0-dBZ ETH alone is not sufficient to extract w profiles from Z profiles.

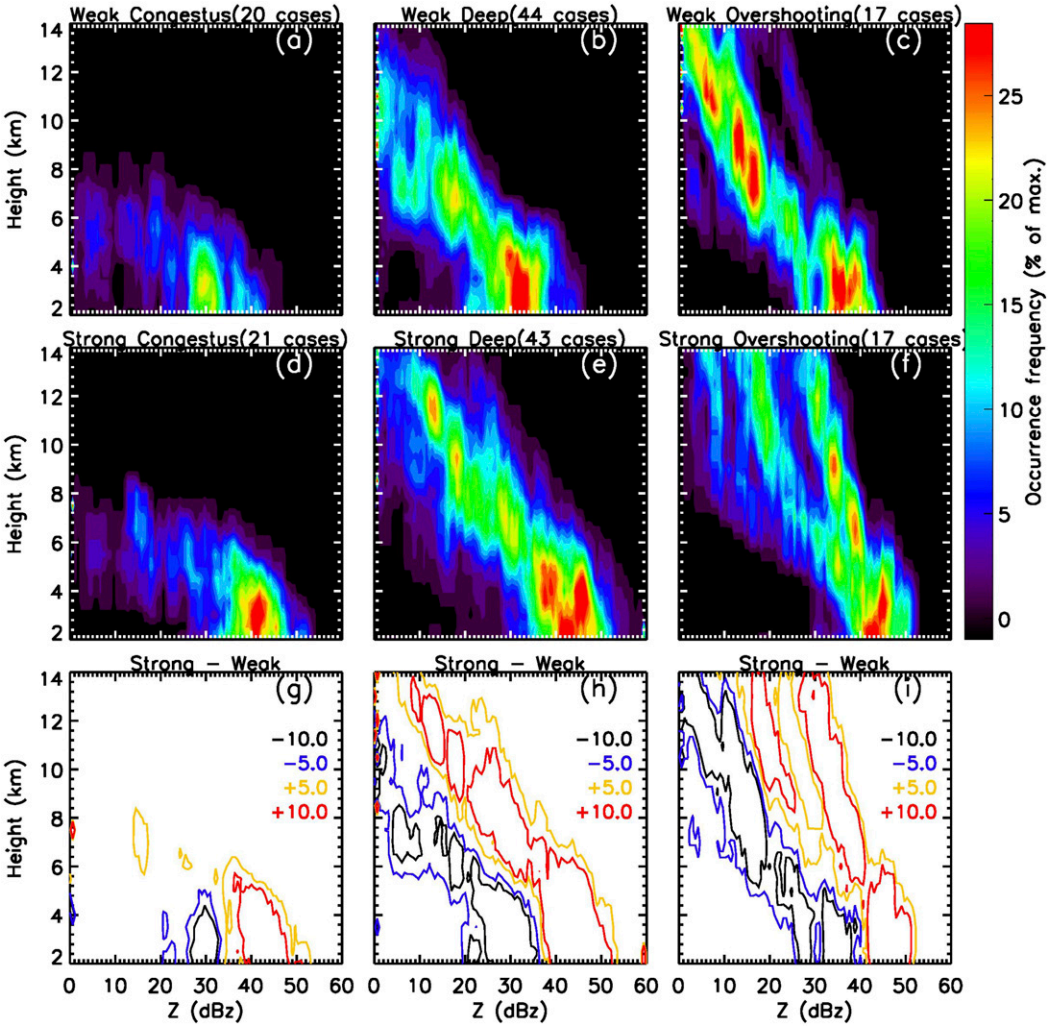

FIG. 3. CFADs of CPOL reflectivities associated with the (a)–(c) weak and (d)–(f) strong cumulus modes for the (left) congestus, (center) deep, and (right) overshooting modes. The weak cumulus clouds had column-mean vertical velocities in the lower tercile (see Fig. 2 for the tercile boundaries), whereas the strong cumulus cloud had column-mean vertical velocities in the upper tercile. A bin size of 1 dBZ in reflectivity and 1.0 km in height is used in these figures. The contoured frequencies in (a)–(f) are normalized by the maximum frequency in each category. (g)–(i) The difference between the corresponding strong and weak cumulus modes.

The observed w profiles' variability in cumulus clouds reaching the same 0-dBZ ETH may be related to where the convective cell is in its life cycle. The mature and decay phase of a convective cell could reach the same 0-dBZ ETH but updrafts are more common in the mature phase and downdrafts dominate the decay phase. The w profiles are also found to be different for the same cumulus cloud type growing in different large-scale atmospheric conditions (e.g., Kumar et al. 2015) and over different underlying surface types (Heymsfield et al. 2010). However, the effects of the large-scale and surface type conditions are not analyzed here because of the limited number of samples and the fixed location of the profiler, respectively. Important is that these conditions do affect the radar reflectivities (Kumar et al. 2013a,b), and therefore these effects will translate into Z profiles' variability.

To identify which CPOL Z profiles' indices relate to the variability in vertical velocity between individual profiles, we first contrast the characteristics of Z profiles associated with ''weak'' and ''strong'' convection for the three cumulus cloud categories (Fig. 3). The weak and strong convection separation is obtained using the lower and upper terciles of the column-mean vertical velocity distribution, respectively. These tercile boundaries are shaded in Fig. 2. This weak/strong separation approach

was proposed and used in Luo et al. (2014). The contoured frequency by altitude diagrams (CFADs; Yuter and Houze 1995) of CPOL reflectivities associated with the six different categories (three cumulus modes, and two convective "strengths" for each mode) are shown in Figs. 3a–f. Figures 3g–i show absolute difference in the normalized contoured frequencies between the weak and strong convection for the different cumulus modes.

The differences in the reflectivity frequencies associated with weak and strong cumulus clouds (Figs. 3g–i) are well marked. This result indicates that stronger convection systematically exhibits higher reflectivity values at all height levels in all cumulus types. This is consistent with the well-known cloud process in convective cores involving convective updrafts, uplift of supercooled water in the ice phase, and latent heat release fueling convective updrafts further. Our results are also consistent with those obtained with A-Train satellite observations in the ice phase (Luo et al. 2014).

Figure 3 demonstrates that indices describing this shift in the Z profiles' distribution toward higher values as convection strength increases should be able to broadly capture the variability in column-mean vertical velocities. To guide the development of relevant reflectivity indices to capture this variability, we construct a composite of w profiles from wind profiler and Z profiles from CPOL for 13 deep convective systems that formed or propagated across the profiler sites (Fig. 4). Note that the dataset used to construct these composites includes both convective and stratiform cloud types, and so it is not same as that used in the previous figures. The criterion used to select these storm events was that the convective system must last at least 30 min within a domain around the profiler, which is set to be a square region consisting of nine CPOL pixels centered over the profiler site (56.25 km^2). However, the composite of reflectivity shown in Fig. 4a is that from the CPOL vertical column directly over the profiler site, not an average of the square region surrounding the profiler. Once a matching convective system was found, its reflectivity profiles are manually inspected to identify the time when the convective cell has fully matured. This time is set as $t = 0$ min for the composite analysis.

The requirement of at least 30 min of contiguous convective profiles at the profiler site implies that mostly wider and therefore deeper convective clouds are captured (e.g., Kumar et al. 2013a). Relaxing the convective time limit produced statistical noise during compositing because of the addition of more frequent short-duration narrow congestus clouds and edges of passing deep clouds. A more conventional technique for selecting storms, provided there is relevant information over the full 3D scanning radar volume, is described in Zuluaga and Houze (2013) but is not applicable to series of vertical profiles. This more accurate approach will be adopted in a subsequent study, when dual-Doppler 3D wind retrievals are produced from a pair of radars around Darwin.

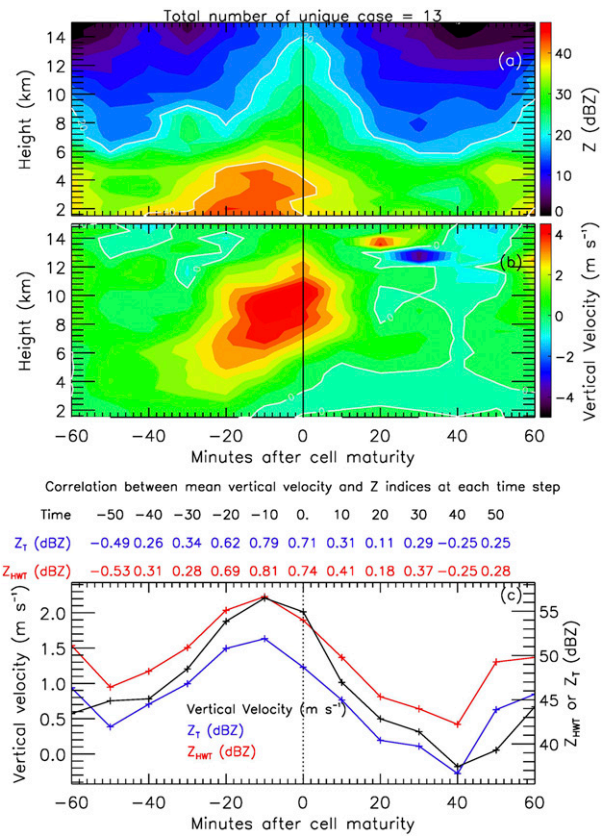

FIG. 4. Composite mean responses of (a) CPOL reflectivities and (b) wind-profiler vertical velocity for up to 1 h on either side of 13 convective storms crossing over the profiler site. The data were averaged in bins of size 10 min in time and 1 km in height. The criteria used to select storms are defined in the text. Apart from near $t = 0$ min, all other times may contain some effects of stratiform clouds. The superimposed white curve in (b) represents the 0 m s^{-1} velocity level. (c) Line plots of temporal evolution of column-mean vertical velocity (black), mean of the column-total reflectivity (Z_T; blue) and mean of the height-weighted column reflectivity totals (Z_{HWT}; red). The tabulated statistics are the correlations between mean velocities and the two reflectivity indices (Z_T, Z_{HWT}) in 10-min bins of cell lifetime. There are at most 13 velocity–reflectivity pairs used to compute the correlations.

Although this composite is not derived from a large number of samples (13 cases only), well-defined structures are readily observed on the composite life cycle (Fig. 4). Based on the conceptual model of storm development described in May et al. (2002), three phases of the storm life cycle can be characterized by different reflectivity and vertical velocity signatures: a growth phase with mostly shallow cumulus (from ~−50 to −20 min),

a mature phase with hail production as riming occurs in the strong updraft above freezing level (from −20 to +20 min), and a decay phase as the gust front cuts off the low-level inflow (from ~+20 to +60 min). The 0°C isotherm is located at about 4.5 km in the Darwin region during the wet season, allowing for a simple discrimination in height between predominantly liquid and predominantly ice phases of convective storms. The growth phase is characterized by a rapid increase in reflectivity below 5-km height associated with the onset of upward motions. In the mature phase, both the updraft strength and the altitude at which the peak updraft strength occurs increase gradually with time. The updraft is strongest above 5-km height, and downdrafts progressively develop below 5-km height. Likewise, the low-level reflectivity peaks during the mature phase and then begins to weaken after $t = 0$ min as rain develops. Above 5-km height, however, 20–30-dBZ echoes are found around $t = 0$ min where the strongest updraft speeds occur. The decay phase is predominantly stratiform precipitation, as indicated by mesoscale downdrafts that are typical of stratiform regions (Fig. 4b). The formation of downdrafts in the mid- to upper troposphere (around $t = 40$ min) is also associated with a drop in radar reflectivity.

Comparing Fig. 4a with Fig. 4b suggests that there is no point-by-point relationship between corresponding Z and w values. However, when viewing these results from a whole column perspective, there is some relationship between Z and w columns. This is illustrated in Fig. 4c, which shows time series averages of two column-based reflectivity indices and column-mean vertical velocity. The first index is a simple sum of reflectivity in linear units (but plotted in decibels) over the whole column (Z_T). The second proposed index is a height-weighted sum of reflectivity Z ($\text{mm}^6\,\text{m}^{-3}$) over the whole column, $Z_{\text{HWT}} = 10\log\sum_{i=1}^{i=\text{nz}} Zh$, where h is in kilometers. The weighting with height allows for the ice part of the reflectivity profile, where updrafts are strongest but reflectivities are lower than in liquid phase in the column because of differences in refractive indices of ice and water, to contribute more to the sum of reflectivities. Correlation coefficients between reflectivity indices and column-mean vertical velocity are calculated at each 10-min interval using the 13 cases used to build the composites shown in Figs. 4a and 4b. Correlation coefficients are higher during the mature phase (from −25 to +5 min), when updrafts are strongest. Smaller correlations are estimated outside the window from −30 to +30 min because of the increase in contribution from stratiform regions. Note again that the effects of stratiform clouds will not be included when parameterizing w profiles from Z profiles, as our goal is to describe convective mass flux. Correlation coefficients between Z_{HWT} and column-mean vertical velocity are slightly better than those obtained with Z_T. This indicates that weighting the ice phase more in the summation has improved the correlation.

Figure 4 shows that Z_{HWT} is a better proxy to capture the variability in column-mean vertical velocity than direct sums of Z, but this inference is based on only 13 deep convective systems. Comparison of the composites of reflectivity and vertical velocity (not shown) further indicates that there is also some correlation between the time evolution of reflectivity dZ/dt and the vertical velocities. In addition, Zipser and Lutz (1994) described a connection between column-mean vertical velocities and the mean vertical gradient of reflectivity dZ/dh. Therefore, in what follows we contrast the correlation coefficients of three reflectivity indices (Z_{HWT}, dZ/dt, and dZ/dh) with the column-mean vertical velocities using the entire two wet seasons' convective population. By this we mean using the entire 246 convective profiles that are used in Figs. 1 and 2 and not including any stratiform profiles.

We also estimated correlations obtained when data points are above or below the 0°C isotherm altitude (around 4.5-km height over Darwin), as such comparisons may provide preliminary insights into the application of such a technique to spaceborne radars operating at attenuating frequencies and observing convection from the top. This important spaceborne application is, however, beyond the scope of this paper, as it would require analyzing the CPOL profilers' conjunctions using exactly the minimum detectable reflectivity of spaceborne precipitation radars (typically 15–20 dBZ).

To estimate the correlations, we first bin the data into 2-km bins of 0-dBZ ETH (the relatively large value of 2 km is used to increase the number of samples in each bin) to examine the relationship between reflectivity and vertical velocity as convection deepens. Then for each bin, we calculate the correlation coefficient between the various column reflectivity indices and the column-mean vertical velocity (Fig. 5). In all 0-dBZ ETH bins, the correlation is highest when using the entire column Z_{HWT} (black). The correlations using Z_{HWT} only below 4.5-km height (blue) are also very similar to those obtained with entire column Z_{HWT} except for the deepest convective clouds. Using Z_{HWT} above 4.5-km height (purple) produces correlations as high as Z_{HWT} but only in deeper convective clouds (0-dBZ ETH exceeding 7 km). The Z_{HWT} above 4.5-km height could therefore potentially be used to approximate the w profiles using spaceborne radar reflectivities at attenuated frequencies (such as *CloudSat*), for which reflectivity below the 0°C isotherm altitude is strongly attenuated. The dZ/dt index

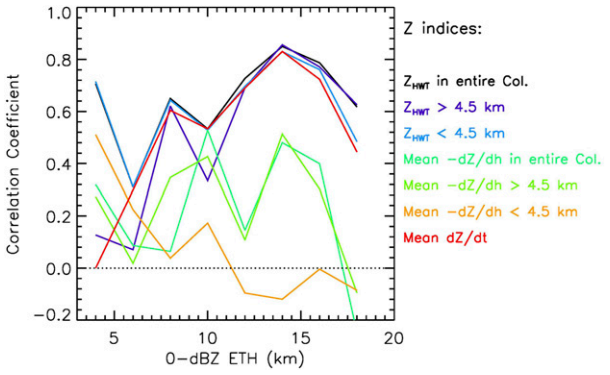

FIG. 5. Correlation coefficient between the profiler column-mean vertical velocities against different CPOL reflectivity indices, as a function of 0-dBZ ETH. The 0-dBZ tops are binned into broad 2-km bins to increase the number of statistics.

(red) is also highly correlated with vertical velocity, except for the congestus clouds.

Overall, Z_{HWT} produces the highest correlations with vertical velocity over the whole 0-dBZ ETH range. It is therefore used in what follows to parameterize the variability of the w profiles in convective clouds. Interestingly, Z_{HWT} is also clearly a much better proxy for vertical velocity variability than the $-dZ/dh$ indices (green and orange) suggested by Zipser and Lutz (1994), which are actually least correlated with vertical velocity among all reflectivity indices tested in Fig. 5.

b. Extraction of w profiles from Z profiles

Results from section 3a show that (i) convective cloud dynamics consist of a dominant updraft component and a weak downdraft component, indicating that updraft and downdraft w profiles can be estimated separately; (ii) the w profiles are very different for the different cumulus modes, therefore the 0-dBZ ETH is a strong constraint on the mean w profiles; and (iii) the variability of the column-mean vertical velocity within each cumulus mode is best correlated with the height-weighted reflectivity index (Z_{HWT}). Using results from section 3a, we now attempt to parameterize updraft and downdraft w profiles using 0-dBZ ETH and Z_{HWT} as inputs. A functional form of the parameterization of w profiles [hereinafter denoted $w(h)$] can be expressed as

$$w(h) = w_U(h)T_Z(h) + w_D(h), \tag{1}$$

where h is height in kilometers, w_U and w_D denote the updraft and downdraft values (m s^{-1}), and T_Z is used to introduce variability to w_U using the Z_{HWT} measurements and is a dimensionless quantity. No such tuning is applied to w_D because the downdraft magnitudes and variability are much smaller than those of the updrafts.

The vertical profiles of w_U are obtained by applying a least squares fit to the mean updraft w profiles for each cumulus mode in Fig. 1:

$$w_U(h) = \begin{cases} 0.040h + 0.992 & \mathrm{ETH} \le 7\,\mathrm{km} \\ -0.002h^4 + 0.052h^3 - 0.571h^2 + 2.700h - 2.735 & 7 < \mathrm{ETH} \le 15\,\mathrm{km} \\ -0.045h^2 + 1.089h - 0.896 & 15\,\mathrm{km} < \mathrm{ETH} \end{cases}. \tag{2}$$

A quartic polynomial is needed to model the complex profile of the deep convective mode (see Fig. 1). In contrast, linear and quadratic polynomials are sufficient for the congestus and overshooting modes, respectively. The equation for w_D is derived in a similar manner, but no separate parameterizations for each cumulus mode is required, as observed in Fig. 1:

$$w_D(h) = 0.0339h^2 + 0.4109h - 1.6852. \tag{3}$$

Building T_Z requires some additional analysis. In what follows we examine how the residual vertical velocities, w_{res} [the difference between the individual profiler column-mean vertical velocity and that derived using (1) with $T_Z = 1$] vary with Z_{HWT}. Figure 6 shows w_{res} as a function of Z_{HWT} for four 2-km bins of 0-dBZ ETH (defined in the same way as in Fig. 5). The remaining four 2-km 0-dBZ ETH bins are not shown for brevity. It is to be noted that in all the 0-dBZ ETH bins shown in Fig. 6, there is a reasonably linear relationship between w_{res} and Z_{HWT}. The slope of the derived linear fits increases with 0-dBZ ETH. Similarly, the y intercepts also show a negative linear relationship with 0-dBZ ETH. These relationships of the y intercepts and slopes extracted for the eight 2-km bins of 0-dBZ ETH, with the 0-dBZ ETH are shown in Figs. 7a and 7b, respectively. A remarkably linear relationship with 0-dBZ ETH is obtained. As a result, the residual vertical velocity w_{res} is modeled as a simple linear function of Z_{HWT}, with the slope and y intercept coefficients of this model a linear function of 0-dBZ ETH:

$$w_{\mathrm{res}} = a + bZ_{\mathrm{HWT}}, \tag{4}$$

with $a = 4.391 - 1.238\mathrm{ETH}$ and $b = -0.061 + 0.021\mathrm{ETH}$.

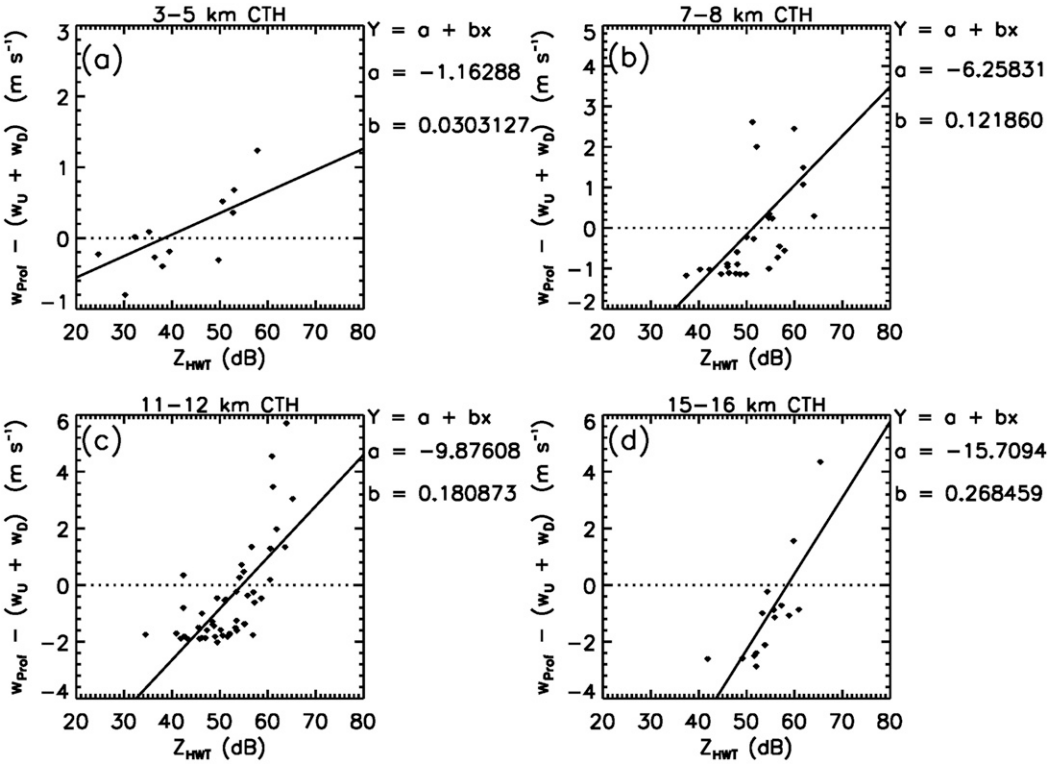

FIG. 6. (a)–(d) Scatterplots of column-mean residual vertical velocity (directly observed by profiler − derived from equation with $T_Z = 1$) against the height-weighted column reflectivity totals (Z_{HWT}) for four 0-dBZ cloud-top bins, each with a bin width of 2 km. The remaining four clouds are not shown in interest of brevity. The sloping lines in these panels are the least squares linear fits of the scatter.

Here w_{res} corresponds to the amount by which the column-mean updraft speed derived from (2) ($\overline{w_U}$) should be adjusted. However, Fig. 4 also shows that both the intensity and the altitude of peak enhancement increased with time approaching $t = 0$ min. During this phase of the storm, Z_{HWT} also increases. Hence, an additional filter is introduced as a multiplying factor to mimic this joint increase in magnitude and height of the updraft peak with increasing Z_{HWT}, which is defined as $[w_U(h)^{0.5}]/[(\overline{w_U})^{0.5}]$. The 0.5 exponent is found to produce the best fit with the observations. Thus T_Z is finally expressed as

$$T_Z = \left(\frac{w_{\mathrm{res}} + \overline{w_U}}{\overline{w_U}}\right)\left[\frac{w_U(h)^{0.5}}{(\overline{w_U})^{0.5}}\right]. \tag{5}$$

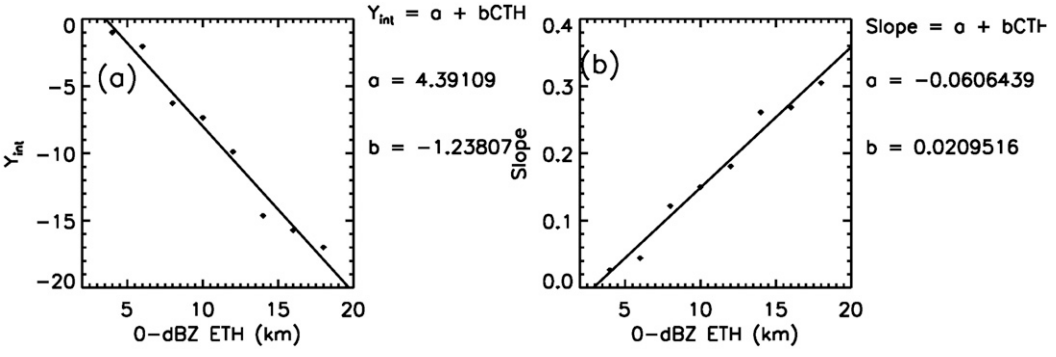

FIG. 7. Scatterplot of (a) y intercept and (b) slope values against the 0-dBZ ETH. These y intercept and slope values are from the results shown in Fig. 6 and also include statistics from the remaining four cloud classes.

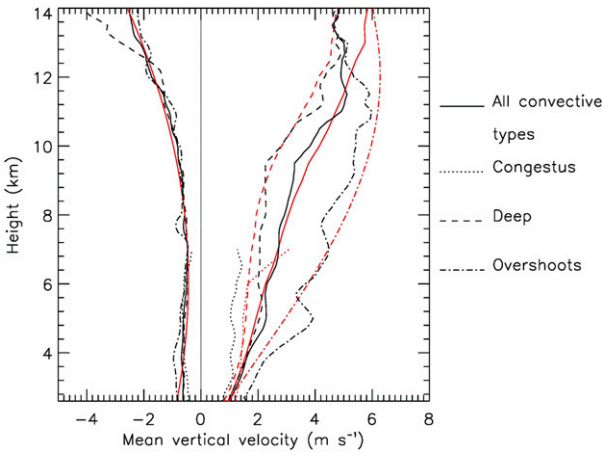

FIG. 8. Profile of mean updraft and downdraft vertical velocity associated with different cumulus cloud modes. The black and red curves in this figure and all subsequent figures represent the wind-profiler and CPOL vertical profiles of radar reflectivity (VPRR)-based vertical velocity trends, respectively.

c. *Evaluation of the Z-profile-based in-cloud vertical velocity*

1) AGAINST THE TRAINING WIND PROFILER OBSERVATIONS

We start a series of evaluation tests to check how well the Z-profile-based vertical velocities approximate the observed velocities. Our reference observational dataset is the dual-frequency wind profiler measurements collected for October 2005–April 2006 and October 2006–April 2007. This is not an independent test, as the same profiler dataset was used to develop the Z-profile-based velocity parameterization. However, it provides a quantitative measurement of how much variability has been lost when developing this parametric representation of vertical velocity. More independent tests will follow in the next two subsections.

The results of the evaluation tests are shown in Figs. 8–10, with a comparison of basic mean vertical profiles of vertical velocities for the three cumulus modes (Fig. 8), followed by an evaluation of the individual column-mean vertical velocity variability in 2-km bins of 0-dBZ ETH (Fig. 9), and finally a comparison of the probability distribution of individual vertical velocity values at each height level (Fig. 10). In these figures, the profiler-determined velocities are in black and those extracted from the Z profiles' parameterization are in red. The subsequent discussion assumes that the profiler measurements are the truth, although they include some retrieval errors (as described in Williams 2012).

There is good agreement between the mean velocity profiles obtained from both techniques for the different cumulus modes (Fig. 8). The largest differences, though less than $1\,\mathrm{m\,s^{-1}}$, occurred near 0-dBZ tops for the congestus mode (dotted curve), and above 12-km height for the deep (dashed curve) and overshooting modes (dotted–dashed curve).

Figure 9 shows a comparison between the observed individual CPOL Z_{HWT}–profiler column-mean vertical velocity pairs (Fig. 9a) and the CPOL Z_{HWT}–Z-profile-based column-mean vertical velocity pairs (Fig. 9b) in 2-km bins of 0-dBZ ETH, as done for Figs. 5 and 6. For each of these 0-dBZ ETH slabs, the Z_{HWT} (bottom dots) and column-mean vertical velocities (top dots) pairs are represented by the short sloping lines. This plot therefore provides a quantitative view of the true observed variability in the Z_{HWT}–column-mean vertical velocity relationship at any given 0-dBZ ETH and how well this variability is captured by the parameterization. The main feature from Fig. 9a is that the relationship between Z_{HWT} and column-mean wind profiler velocities is highly organized, which further confirms the potential of using Z_{HWT} to capture the variability of vertical velocity as noted in section 3a. The parameterized vertical velocities (red circles in Fig. 9b) are indeed able to capture most of the variability observed in the profiler velocities (black circles in Fig. 9b), except for some very large values.

Figure 10 shows the probability distribution function (PDF) of profiler and CPOL Z-profile-based vertical velocities in 1-km-height bins. This comparison shows that the parameterization marginally overestimates the 50th percentile and marginally underestimates the 75th percentile of vertical velocity compared to wind profiler retrievals. Focusing now on the extremes, the parameterization tends to overestimate the 10th percentile and underestimate the 90th percentile of the distribution. Overall, this indicates that the parameterization does represent fairly well the PDF of vertical velocity with, however, a slight underestimation of its width.

From the results shown in Figs. 8–10, our preliminary conclusion is that the parameterization of vertical velocities using Z-profile-based indices is capable of reproducing mean vertical velocities retrieved with the dual-frequency wind profiler technique. However, the parametric model tends to underestimate the incidence of upper and lower velocity extremes. The evaluation discussed above made use of the same dataset as that used to develop the parameterization. So in the next two subsections, we conduct more independent assessments.

2) AGAINST THE 2009–10 WIND PROFILER DATA

We now test the performance of the Z-profile-based velocity retrievals on another wet season (2009/10) of wind profiler velocity retrievals. A total of fifty-eight

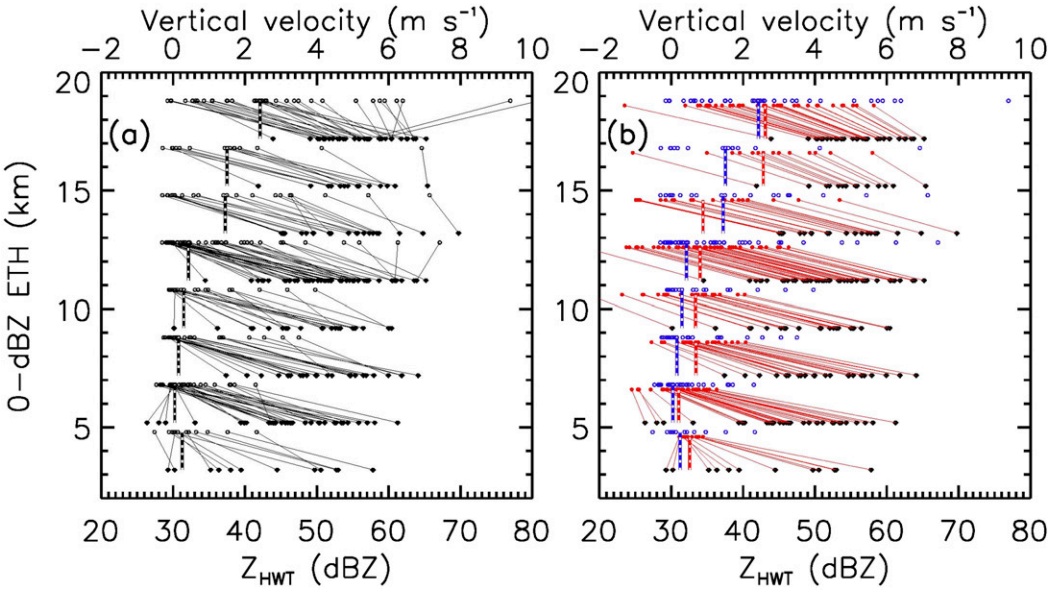

FIG. 9. (a) Scatterplots of Z_{HWT} (primary x axis) against wind-profiler column-mean vertical velocity (secondary x axis) in 2-km bins of 0-dBZ ETH. (b) As in (a), but the vertical velocities are obtained from CPOL VPRR. Unfilled purple circles in (b) are wind-profiler vertical velocity means and have been overplotted for easier comparison with VPRR-based velocity means (filled red circles). The thick dashed purple and red vertical lines are the median of velocities from wind-profiler and VPRR-based vertical velocities, respectively.

10-min convective columns are detected for this wet season. The aforementioned statistical comparisons (Figs. 8–10) when repeated with this profiler dataset produced similar results. To summarize, we show in Fig. 11 a scatterplot (dotted) of parameterized velocities against the profiler velocities from matching time–height convective bins of size 10 min in time and 1 km in height. The same information for the training dataset (2005–07) is shown by the solid contour lines in Fig. 11, which represent the 2D histogram of points. The red vertical bars show mean ± one standard deviation ranges as a function of the observed profiler vertical velocity using dataset from entire three wet seasons.

Notably, the performance of the Z-profile-based velocity tool for the two separate profiler datasets is very similar, and therefore increases the confidence that the w-profile parameterization is representative of more than just the training dataset. As discussed in section 3c(1), Fig. 11 also reveals that Z-profile-based retrievals are underestimating large vertical velocities. How this bias in the parameterized velocities affects the mass-flux computation is discussed in section 4.

3) AGAINST A 1-MONTH DATASET OF DUAL-DOPPLER VERTICAL VELOCITY RETRIEVALS

The dual-Doppler retrievals used in this study are based on a variational approach (described in Protat and Zawadzki 1999; Collis et al. 2013), whereby the 3D winds are obtained by minimizing the difference between the observed radial winds from a Doppler radar pair (CPOL and Berrimah radars in our case) and ensuring that the three wind components satisfy the

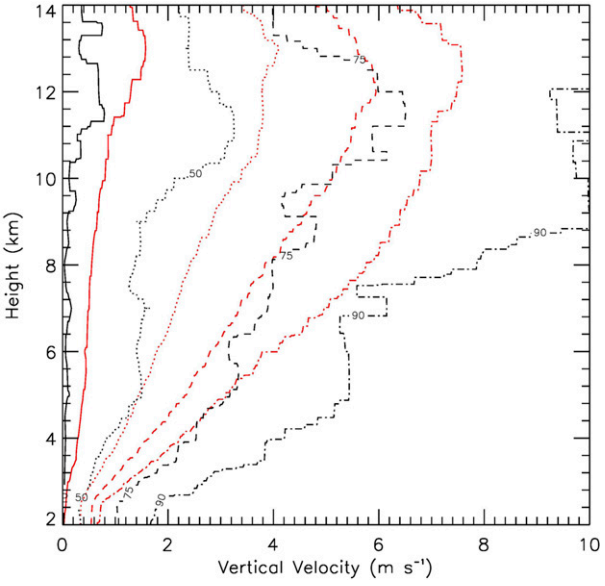

FIG. 10. 2D cumulative probability distribution of wind-profiler (black) and CPOL VPRR-based vertical updraft velocities (red). The curves are the 10th (solid), 50th (dotted), 75th (dashed), and 90th (dotted–dashed) percentiles of vertical velocity frequencies as a function of height.

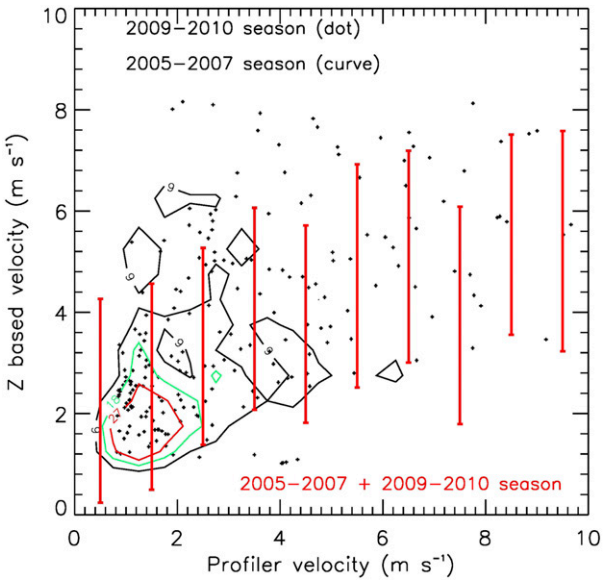

FIG. 11. Scatterplot of VPRR-based vertical velocities against wind-profiler velocities using data from October 2009 to April 2010. Data points from matching 10-min bins in time and 1-km bins in height were used in the scatterplot. The overplotted contour curves are the 2D histogram of scatter for the velocity data from the 2005–07 wet seasons. The red scatter bars use the entire three wet seasons of dataset and represent ± one std dev about the means.

anelastic approximation of the mass continuity equation. Typical assumptions made in dual-Doppler techniques, such as the vertical velocity at cloud base and top being $0\,\mathrm{m\,s^{-1}}$, and fall speed corrections on the observed Doppler winds, may hinder the accuracy of the dual-Doppler retrievals to some unknown extent. Unfortunately, the Darwin wind profiler is located just outside of the dual-Doppler retrieval regions (along the baseline formed by the two radars), thus it is not possible to directly cross validate the dual-Doppler retrievals with the profiler measurements. However, Collis et al. (2013) have shown on a few case studies that these two estimates of vertical velocity were in good agreement. The gradient of a linear fit of profiler velocities against dual-Doppler velocities was 0.83 with a correlation coefficient of 0.85.

The advantage of comparing the *Z*-profile-based retrievals with the dual-Doppler vertical velocity retrievals is that the number of convective pixels increases substantially compared to profiler retrievals, as the parameterization can be applied to any convective pixel that is within the large dual-Doppler retrieval region. The downside is that the dual-Doppler vertical velocities are presumably not as accurate as the wind profiler retrievals. Using a month of comparisons, there are a total of 21 365 convective columns for which dual-Doppler and *Z*-profile-based vertical velocity retrievals are available.

Figures 12a–c, which are created in the same way as the contour lines in Fig. 11, show the frequency distribution of vertical velocities obtained from the *Z*-profile-based technique against the dual-Doppler approach for the congestus, deep, and overshooting cumulus modes, respectively. To further explore the comparability between these two velocity retrieval approaches as a function of height, the superimposed colored contours show the 50th percentiles of the *Z*-profile-based velocities are plotted against dual-Doppler velocities in different height slabs. These results shows that the agreement between the velocities is highest below 5 km, followed by between 5 and 10 km, and are the lowest between 10 and 15 km, regardless of the cumulus cloud mode. Thus the discrepancy between the two approaches is most obvious for the overshooting mode. The velocity parameterization is tuned with wind profiler measurements, and both show the updraft intensities are strongest between 10 and 15 km (Fig. 8). Other ground-based and airborne wind profiler observations also found similar characteristics in w profiles associated with deep convection (e.g., May and Rajopadhyaya 1999; Heymsfield et al. 2010; Giangrande et al. 2013). However, ground profilers may undersample the upper regions of the convective cores, in particular those for which the reflectivities are less intense, because of the drop in sensitivity of the profiler with height. Another reason for the observed discrepancy in the upper levels could be due to the assumption made in the dual-Doppler retrieval that the vertical velocity at cloud top is $0\,\mathrm{m\,s^{-1}}$. True cloud-top heights are usually few kilometers higher than those observed with C-band radars.

4. Convective mass flux

The main motivation for developing a scanning radar reflectivity-based vertical velocity parameterization is to produce quantitative estimates of mass flux on scales directly relevant to GCMs (currently around 100-km horizontal resolution). Current GCMs, especially those used for climate studies, cannot resolve convective-scale motions and will not for the foreseeable future, as the explicit representation of convection requires horizontal resolutions of 1 km or less. Therefore a cumulus parameterization, such as the widely used convective mass-flux scheme, will still be required for many years to represent the collective effects of an ensemble of convective cells within a GCM grid box. The evaluation of mass-flux schemes with observations has proven difficult because of a lack of relevant long-term quantitative

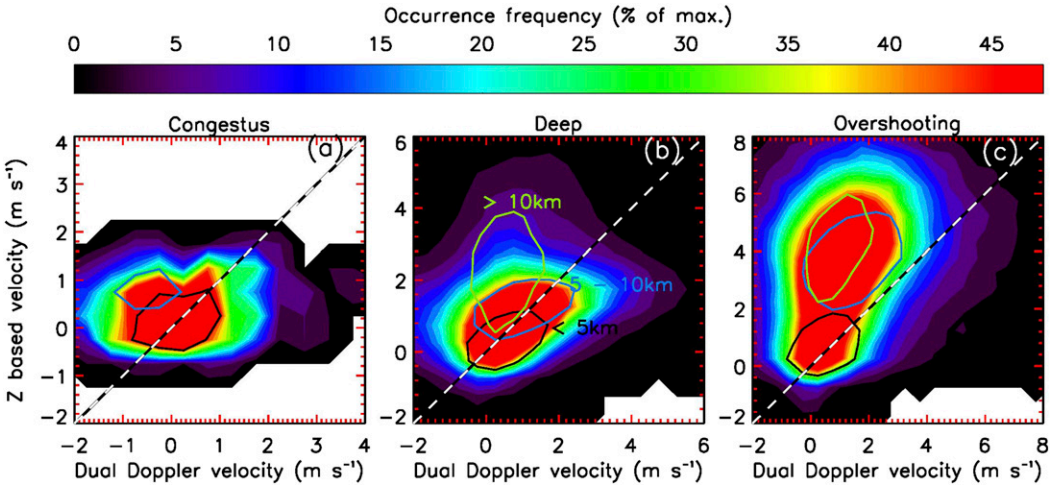

FIG. 12. 2D Histogram of VPRR-based vertical velocity and dual-Doppler vertical velocities using data from matching 10-min bins in time and 1-km bins in height over the 1 month with dual-Doppler retrievals. The colored contour curves are the 50th percentiles using data from different height regions: below 5 km (black), between 5 and 10 km (blue), and above 10 km (green).

vertical velocity datasets within cumulus clouds. Previous efforts combined network of surface rainfall observations and vertical air sounding profiles of temperature and humidity, with continuity equations for mass, heat, and moisture to estimate large-scale cumulus mass flux (e.g., Wu 2012 and references therein). In our previous study (Kumar et al. 2015) we used the dual-frequency profiler retrievals of vertical velocity to characterize the mean properties of convective mass flux and its variability as a function of the large-scale environment; however, these results were not readily useful for GCM verification, as this requires long time series of individual mass-flux profiles. The present study attempts to bridge this gap by deriving profiles of convective mass flux at a typical GCM grid resolution from measured CPOL convective area fraction and convective vertical velocity retrieved using the parametric representation of section 3 applied to 3D CPOL reflectivities.

Figure 13 shows a comparison of such mass-flux profiles for the different cumulus modes using the vertical velocity measurement from the wind profiler (black) and using the Z-profile-based parameterization (red). In these mass-flux computations, the convective area fraction is the same, so only the errors in vertical velocity make up for the differences between the mass-flux profiles. The approach used to compute mass flux on scales relevant to GCMs using the vertical-pointing profiler observations has been described in Kumar et al. (2015). They calculated the convective area fractions from the single-column observations using a temporal aggregation approach, which is defined as the ratio of the time CPOL identifies convection above the profiler over the total sampling time. The same approach has been used here.

As seen in Fig. 13, the mean mass-flux profiles derived from the parameterization do match the reference profiles quite well, except for the congestus mode for which the parameterized mass flux is too large. As noted in section 3c, a shortfall in the parameterized vertical velocities is the underestimation of the velocity extremes. Next we show how the errors in vertical velocity translate into errors in mass flux. Cumulus mass flux is the

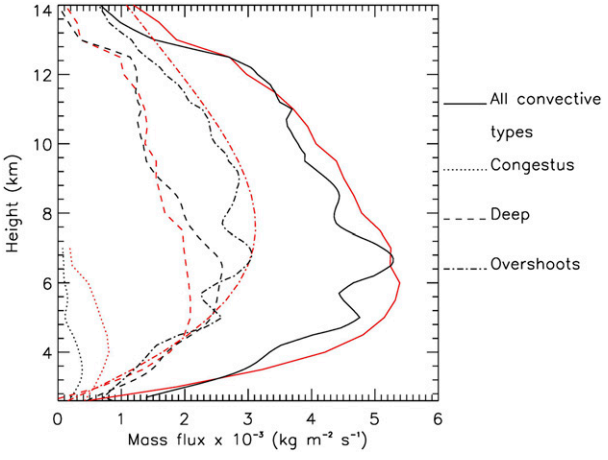

FIG. 13. Two wet seasons' mean mass flux associated with all cumulus clouds (solid curves), congestus (dotted), deep (dashed), and overshooting convection (dotted–dashed) using wind-profiler (black) and CPOL-based (red) measurements taken at the profiler site. The procedure used to compute mass flux from these single-column observations is described in the text.

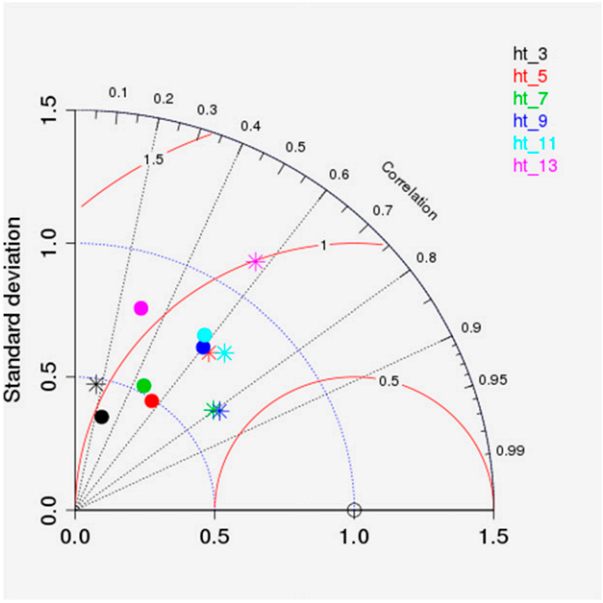

FIG. 14. Taylor diagram displaying a statistical comparison between observed vertical velocity–mass flux and CPOL VPRR-based vertical velocity–mass flux at six different heights. The vertical velocity values are represented by filled circles, and corresponding mass-flux values are shown with asterisks. As explained in the text, all standard deviations (both observed and parameterized) are divided by the appropriate observed standard deviation so that all observed standard deviations are at the coordinate of (1.0, 0) (unfilled circle). Refer to Table 1 for the raw observed standard deviations.

product of three variables, air density, convective area fraction, and vertical velocity. Convective area fraction is a direct observation, so errors are expected to be much lower compared to those from the parameterized w profiles. This implies that errors in mass flux are likely to be lower than those in velocities. These errors on vertical velocity (filled circles) and convective mass flux (asterisks) are characterized in Fig. 14 using a Taylor diagram (Taylor 2001). Since the observed vertical velocities and mass fluxes are characterized by different standard deviations, and the standard deviations also change with height, all the model values are normalized by the reference data standard deviations (blue ring at value 1). The absolute values of the standard deviations are given in Table 1. The red rings on the Taylor diagram correspond to root-mean-square (RMS) differences between the modeled and retrieved data divided by the standard deviation. For instance, the location of the pink asterisk on the Taylor diagram indicates that for heights between 12 and 14 km, the correlation between modeled and profiler-retrieved mass fluxes is 0.59, the RMS difference is $1 \times 0.083\,\mathrm{kg\,m^{-2}\,s^{-1}}$, and the standard deviation of modeled mass flux is 1.15 higher than that of the observed mass flux.

TABLE 1. Wind profiler observed vertical velocity and mass flux standard deviations at six different height levels.

Height (km)	Std dev of observed vertical velocity ($\mathrm{m\,s^{-1}}$)	Std dev of observed mass flux ($\mathrm{kg\,m^{-2}\,s^{-1}}$)
3	1.92	0.123
5	2.24	0.125
7	3.13	0.184
9	2.75	0.198
11	2.87	0.156
13	2.67	0.083

It is evident (Fig. 14) that the parameterization of vertical velocity performs best between 8 and 12 km, with correlations of about 0.6 and normalized standard deviations and normalized RMS differences of about 0.8. Importantly, parameterized mass fluxes systematically score better than parameterized vertical velocities. The lowest correlations and normalized standard deviations are found between 2- and 4-km height. This is because the observed upward velocities drop between 2 and 3 km followed by a steady increase thereon, but our parametric model does not account for this in order to keep the model equation simple (see Fig. 8). Lower vertical velocity correlations in the uppermost layer (12–14 km) are probably due to fewer profiler observations (associated with the drop in sensitivity of the profiler with range), as discussed previously. It is interesting to note that in this uppermost layer the mass-flux correlations and normalized standard deviations are better than those for vertical velocity. This is due to the fact that the convective area fractions are much lower higher up, resulting in fewer errors on mass flux than on vertical velocities.

The main rationale for parameterizing convective mass flux from radar reflectivity only is that it offers the opportunity to characterize the variability of convective mass flux over the life cycle of tropical convection and as a function of the large-scale environmental conditions, which can in turn be used to assess if the GCM mass-flux parameterization captures this variability. To illustrate this potential, Fig. 15 shows a time series of selected convective parameters during the Tropical Warm Pool–International Cloud Experiment (TWP-ICE), at Darwin, Australia (May et al. 2008). Figure 15a shows time series of convectively available potential energy (CAPE; black) and domain mean convective rain rate (red), which describes the convective activity during TWP-ICE. The TWP-ICE period consisted of three different large-scale conditions (e.g., Varble et al. 2011; Davies et al. 2013): an active monsoon period (before day 25, which is 25 January 2006) characterized by strong large-scale upward motions (ω) associated

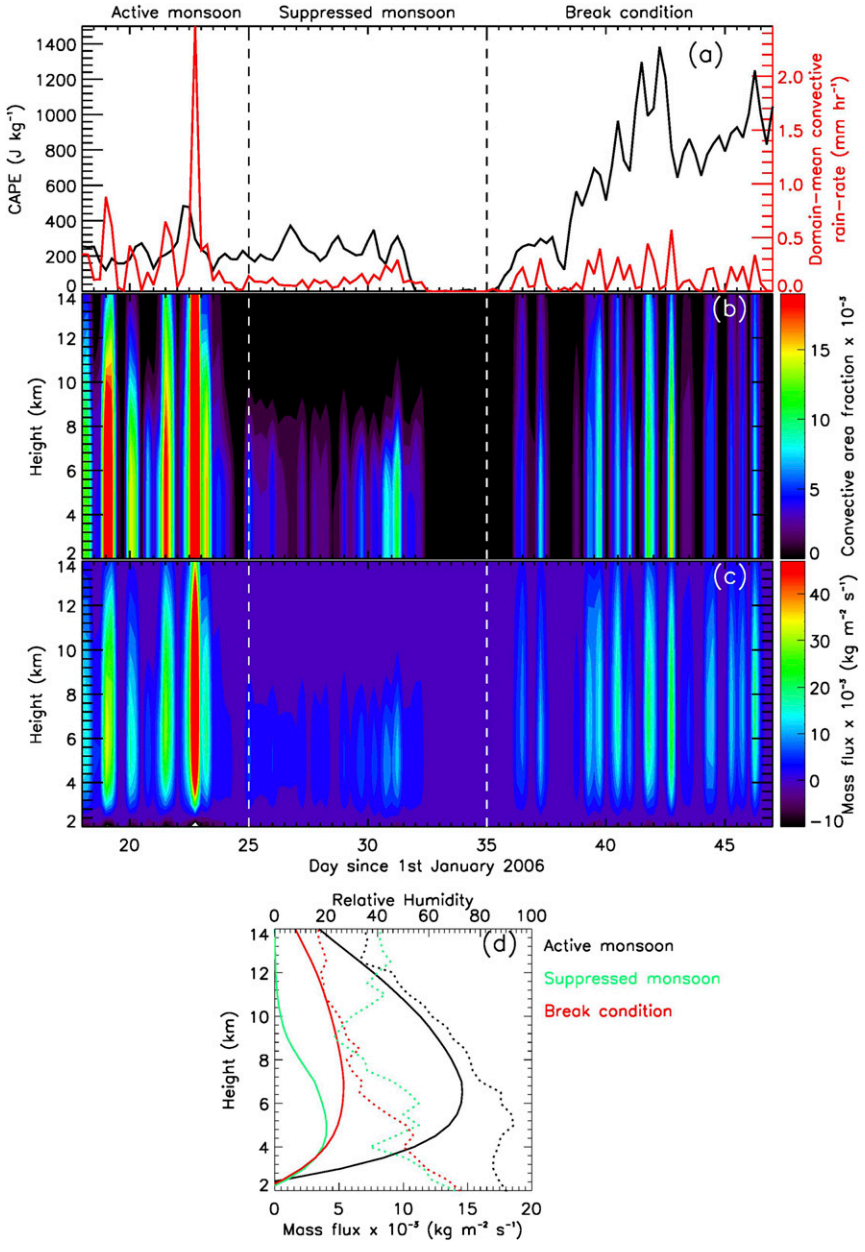

FIG. 15. Time series of (a) CAPE from radiosounding and CPOL domain-mean convective rain rate, (b) CPOL domain-mean convective area fraction, and (c) CPOL VPRR-based mass flux. As explained in the text, the area fraction is calculated using standard spatial approach, and mass flux is product of respective mean area fraction, mean parameterized ω, and air density. Data shown are for the TWP-ICE period (19 Jan–14 Feb 2006) at Darwin. (d) The mean vertical profile of mass flux (solid curves) and relative humidity (dotted curves) associated with the three large-scale conditions, namely, active monsoon (black), suppressed monsoon (green), and break (red) conditions, experienced during the TWP-ICE.

with two major mesoscale convective systems (19–20 and 23–24 January) passing over the CPOL domain was followed by a suppressed monsoon period associated with downward large-scale motions (26 January–2 February) and least rainfall amounts, followed then by break conditions (after 3 February), dominated by diurnally driven alternating large-scale upward and downward motions and strong CAPE.

The associated time–height plots of convective area fraction (Fig. 15b) and mass flux (Fig. 15c) reveal

a noticeable difference between the three large-scale conditions. Note unlike in Fig. 13 where we approximated the convective area fraction using a temporal approach (space–time conversion), in Fig. 15 the area fraction is directly calculated using the conventional spatial approach of the ratio of the coverage area of all convective cells in the CPOL domain over the total CPOL domain of ~44 000 km^2. The method to derive mass flux remains unchanged: at any given height and time, it is the product of mean convective area fraction, mean of parameterized ω of all convective pixels, and air density. The two MCSs during the active monsoon period are associated with highest amounts of convective area fraction and mass flux. The suppressed monsoon period contains shallow convection with convective tops mostly below 8-km height and weaker mass fluxes than during the active monsoon period, with no clear diurnal signal. In contrast, the break period exhibits strong diurnal perturbations in convective area fraction and mass flux, similar to that of convective rain rate (Fig. 15a). A direct comparison of the mean vertical profiles of mass flux during the three large-scale conditions is shown in Fig. 15d. All the mass-flux profiles peak at or within few kilometers above the freezing level (~5 km). The mass flux drops the slowest with height above the peak height in the break period and quickest in the active monsoon period. These mass-flux profiles are consistent with the typical picture of convection in break and monsoonal conditions (e.g., Kumar et al. 2013a,b), with the former characterized by a quick transition from afternoon shallow congestus clouds to deep convection within few hours triggered by local sea-breeze effects and the latter characterized by widespread occurrence of weak shallow convection associated with the monsoon trough, with only a few growing into deep convective towers.

The example shown in Fig. 15 confirms our suggestion that the mass-flux values obtained using the parameterized velocities combined with directly observed convective area fraction are likely of sufficient quality for the first-order evaluation of cumulus parameterizations in GCMs. This provides an exciting opportunity to use our technique to derive mass-flux profiles at a number of locations that host rain radars. It is worth noting, however, that more confidence in the technique should be gained by extending its evaluation performed here to other sites.

5. Summary and future works

This paper describes how C-band radar reflectivities can potentially be used to estimate vertical velocity and mass flux in tropical cumulus clouds in a way that would allow long-term datasets to be constructed at radar locations with a possible global extension using satellite-based reflectivity measurements. We used two wet seasons of vertical profiles of vertical velocities (w profiles) extracted from the Darwin dual-frequency wind profiler pair and collocated vertical profiles of radar reflectivities (Z profiles) from the Darwin C-band polarimetric research radar to develop a parametric model of vertical velocity using only CPOL reflectivity indices. A statistical analysis of profiler w profiles as functions of different properties of CPOL Z profiles from convective intervals revealed that it is possible to parameterize w profiles in cumulus clouds using two Z-profile-based indices: the 0-dBZ ETH to constrain the mean convective w profiles, and the "height-weighted column reflectivity (Z_{HWT})" to constrain the variability of the convective w profiles. The evaluation of the parameterized vertical velocities using the training dataset and two independent datasets demonstrates that vertical velocity values can be estimated accurately up to their 75th percentile but with some underestimation of the extreme values. Furthermore, the product of the parameterized w profiles and the directly observed profile of convective area fraction from the ground-based radar network will be valuable to fully characterize mass flux and its sources of variability to improve the simulation of convection by GCMs. It was noted that the influence of errors made in parameterizing velocities is actually reduced in the mass-flux calculations because the less accurate velocity extremes occur in the upper levels, where both the convective area fraction and air density are small. This parametric representation of the convective w profiles can potentially be applied to any non-Doppler, non-dual-polarization radar, including spaceborne radars, with some adaptations. So there is a potential for much broader use of such simple approach. However, more studies are clearly needed to investigate how variable this relationship is as a function of geographical location, even within the tropical belt, and to adapt it to different minimum detectable radar reflectivities. As more long-term vertical velocity datasets are produced worldwide by the research community, we will ascertain how robust these w parameterizations are outside of the Darwin area and will be able to refine the concept proposed in this study.

Acknowledgments. This work has been supported by the U.S. Department of Energy ARM Program (DE-FG02-09ER64742) and ARC Centre of Excellence for Climate System Science. We acknowledge the contributions of Brad Atkinson and Michael Whimpey in supporting the Darwin observatory and data management.

REFERENCES

Anderson, N. F., C. A. Grainger, and J. L. Stith, 2005: Characteristics of strong updrafts in precipitation systems over the central tropical Pacific Ocean and in the Amazon. *J. Appl. Meteor.*, **44**, 731–738, doi:10.1175/JAM2231.1.

Arakawa, A., 2004: The cumulus parameterization problem: Past, present, and future. *J. Climate*, **17**, 2493–2525, doi:10.1175/1520-0442(2004)017<2493:RATCPP>2.0.CO;2.

Bringi, V. N., T. D. Keenan, and V. Chandrasekar, 2001: Correcting C-band radar reflectivity and differential reflectivity data for rain attenuation: A self-consistent method with constraints. *IEEE Trans. Geosci. Remote Sens.*, **39**, 1906–1915, doi:10.1109/36.951081.

Byers, H. R., and R. R. Braham, 1949: The thunderstorm. U.S. Weather Bureau Thunderstorm Project Rep., 287 pp.

Casey, S. P. F., E. J. Fetzer, and B. H. Kahn, 2012: Revised identification of tropical oceanic cumulus congestus as viewed by CloudSat. *Atmos. Chem. Phys.*, **12**, 1587–1595, doi:10.5194/acp-12-1587-2012.

Collis, S., A. Protat, P. T. May, and C. Williams, 2013: Statistics of storm updraft velocities from TWP-ICE including verification with profiling measurements. *J. Appl. Meteor. Climatol.*, **52**, 1909–1922, doi:10.1175/JAMC-D-12-0230.1.

Davies, L., C. Jakob, P. T. May, V. V. Kumar, and S. Xie, 2013: Relationships between the large-scale atmosphere and the small-scale state for Darwin, Australia. *J. Geophys. Res. Atmos.*, **118**, 11 534–11 545, doi:10.1002/jgrd.50645.

Fierro, A. O., J. M. Simpson, M. A. LeMone, J. M. Straka, and B. F. Smull, 2009: On how hot towers fuel the Hadley cell: An observational and modeling study of line-organized convection in the equatorial trough from TOGA COARE. *J. Atmos. Sci.*, **66**, 2730–2746, doi:10.1175/2009JAS3017.1.

Giangrande, S. E., S. Collis, J. Straka, A. Protat, C. Williams, and S. Krueger, 2013: A summary of convective-core vertical velocity properties using ARM UHF wind profilers in Oklahoma. *J. Appl. Meteor. Climatol.*, **52**, 2278–2295, doi:10.1175/JAMC-D-12-0185.1.

Heymsfield, G. M., L. Tian, A. J. Heymsfield, L. Li, and S. Guimond, 2010: Characteristics of deep tropical and subtropical convection from nadir-viewing high-altitude airborne Doppler radar. *J. Atmos. Sci.*, **67**, 285–308, doi:10.1175/2009JAS3132.1.

Hjelmfelt, M. R., H. D. Orville, R. D. Roberts, J. P. Chen, and F. J. Kopp, 1989: Observational and numerical study of a microburst line-producing storm. *J. Atmos. Sci.*, **46**, 2731–2743, doi:10.1175/1520-0469(1989)046<2731:OANSOA>2.0.CO;2.

Keenan, T. D., K. Glasson, F. Cummings, T. S. Bird, J. Keeler, and J. Lutz, 1998: The BMRC/NCAR C-band polarimetric (CPOL) radar system. *J. Atmos. Oceanic Technol.*, **15**, 871–886, doi:10.1175/1520-0426(1998)015<0871:TBNCBP>2.0.CO;2.

Kumar, V. V., C. Jakob, A. Protat, P. T. May, and L. Davies, 2013a: The four cumulus cloud modes and their progression during rainfall events: A C-band polarimetric radar perspective. *J. Geophys. Res. Atmos.*, **118**, 8375–8389, doi:10.1002/jgrd.50640.

——, A. Protat, P. T. May, C. Jakob, G. Penide, S. Kumar, and L. Davies, 2013b: On the effects of large-scale environment and surface conditions on convective cloud characteristics over Darwin, Australia. *Mon. Wea. Rev.*, **141**, 1358–1374, doi:10.1175/MWR-D-12-00160.1.

——, ——, C. Jakob, and P. T. May, 2014: On atmospheric regulation of the growth of moderate to deep cumulonimbus in a tropical environment. *J. Atmos. Sci.*, **71**, 1105–1120, doi:10.1175/JAS-D-13-0231.1.

——, C. Jakob, A. Protat, C. R. Williams, and P. T. May, 2015: Mass-flux characteristics of tropical cumulus clouds from wind profiler observations at Darwin, Australia. *J. Atmos. Sci.*, **72**, 1837–1855, doi:10.1175/JAS-D-14-0259.1.

Laroche, S., and I. Zawadzki, 1994: A variational analysis method for retrieval of three-dimensional wind field from single-Doppler radar data. *J. Atmos. Sci.*, **51**, 2664–2682, doi:10.1175/1520-0469(1994)051<2664:AVAMFR>2.0.CO;2.

LeMone, M. A., and E. J. Zipser, 1980: Cumulonimbus vertical velocity events in GATE. Part I: Diameter, intensity and mass flux. *J. Atmos. Sci.*, **37**, 2444–2457, doi:10.1175/1520-0469(1980)037<2444:CVVEIG>2.0.CO;2.

Lu, M.-L., Y. Liu, S. Niu, and A. M. Vogelmann, 2012: Observed impacts of vertical velocity on cloud microphysics and implications for aerosol indirect effects. *Geophys. Res. Lett.*, **39**, L21808, doi:10.1029/2012GL053599.

Luo, Z. J., J. Jeyaratnam, S. Iwasaki, H. Takahashi, and R. Anderson, 2014: Convective vertical velocity and cloud internal vertical structure: An A-Train perspective. *Geophys. Res. Lett.*, **41**, 723–729, doi:10.1002/2013GL058922.

Marwitz, J. D., 1973: Trajectories within the weak echo regions of hailstorms. *J. Appl. Meteor.*, **12**, 1174–1182, doi:10.1175/1520-0450(1973)012<1174:TWTWER>2.0.CO;2.

May, P. T., and D. K. Rajopadhyaya, 1999: Vertical velocity characteristics of deep convection over Darwin, Australia. *Mon. Wea. Rev.*, **127**, 1056–1071, doi:10.1175/1520-0493(1999)127<1056:VVCODC>2.0.CO;2.

——, A. R. Jameson, T. D. Keenan, P. E. Johnston, and C. Lucas, 2002: Combined wind profiler/polarimetric radar studies of the vertical motion and microphysical characteristics of tropical sea-breeze thunderstorms. *Mon. Wea. Rev.*, **130**, 2228–2239, doi:10.1175/1520-0493(2002)130<2228:CWPPRS>2.0.CO;2.

——, J. H. Mather, G. Vaughan, C. Jakob, G. M. McFarquhar, K. N. Bower, and G. G. Mace, 2008: The Tropical Warm Pool International Cloud Experiment. *Bull. Amer. Meteor. Soc.*, **89**, 629–645, doi:10.1175/BAMS-89-5-629.

Protat, A., and I. Zawadzki, 1999: A variational method for real-time retrieval of three-dimensional wind field from multiple-Doppler bistatic radar network data. *J. Atmos. Oceanic Technol.*, **16**, 432–449, doi:10.1175/1520-0426(1999)016<0432:AVMFRT>2.0.CO;2.

Ryzhkov, A. V., M. R. Kumjian, S. M. Ganson, and A. P. Khain, 2013: Polarimetric radar characteristics of melting hail. Part I: Theoretical simulations using spectral microphysical modeling. *J. Appl. Meteor. Climatol.*, **52**, 2849–2870, doi:10.1175/JAMC-D-13-073.1.

Shapiro, A., P. Robinson, J. Wurman, and J. Gao, 2003: Single-Doppler velocity retrieval with rapid scan radar data. *J. Atmos. Oceanic Technol.*, **20**, 1758–1775, doi:10.1175/1520-0426(2003)020<1758:SVRWRR>2.0.CO;2.

Spoden, P. J., R. A. Wolf, and L. R. Lemon, 2012: Operational uses of spectrum width. *Electron. J. Severe Storms Meteor.*, **7** (2). [Available online at http://www.ejssm.org/ojs/index.php/ejssm/article/view/86/70.pdf.]

Steiner, M., R. A. Houze Jr., and S. E. Yuter, 1995: Climatological characterization of three-dimensional storm structure from operational radar and rain gauge data. *J. Appl. Meteor.*, **34**, 1978–2007, doi:10.1175/1520-0450(1995)034<1978:CCOTDS>2.0.CO;2.

Taylor, K. E., 2001: Summarizing multiple aspects of model performance in a single diagram. *J. Geophys. Res.*, **106**, 7183–7192, doi:10.1029/2000JD900719.

Varble, A., and Coauthors, 2011: Evaluation of cloud-resolving model intercomparison simulations using TWP-ICE observations: Precipitation and cloud structure. *J. Geophys. Res.*, **116**, D12206, doi:10.1029/2010JD015180.

Williams, C. R., 2012: Vertical air motion retrieved from dual-frequency profiler observations. *J. Atmos. Oceanic Technol.*, **29**, 1471–1480, doi:10.1175/JTECH-D-11-00176.1.

Wu, T., 2012: A mass-flux cumulus parameterization scheme for large-scale models: Description and test with observations. *Climate Dyn.*, **38**, 725–744, doi:10.1007/s00382-011-0995-3.

Yuter, S. E., and R. A. Houze, 1995: Three-dimensional kinematic and microphysical evolution of Florida cumulonimbus. Part II: Frequency distributions of vertical velocity, reflectivity, and differential reflectivity. *Mon. Wea. Rev.*, **123**, 1941–1963, doi:10.1175/1520-0493(1995)123<1941:TDKAME>2.0.CO;2.

Zipser, E. J., 2003: Some view on ''hot towers'' after 50 years of tropical field programs and two years of TRMM data. *Cloud Systems, Hurricanes, and the Tropical Rainfall Measuring Mission (TRMM)*, *Meteor. Monogr.*, No. 53, Amer. Meteor. Soc., 49–58, doi:10.1175/0065-9401(2003)029<0049:CSVOHT>2.0.CO;2.

——, and K. R. Lutz, 1994: The vertical profile of radar reflectivity of convective cells: A strong indicator of storm intensity and lightning probability? *Mon. Wea. Rev.*, **122**, 1751–1759, doi:10.1175/1520-0493(1994)122<1751:TVPORR>2.0.CO;2.

Zuluaga, M. D., and R. A. Houze Jr., 2013: Evolution of the population of precipitating convective systems over the equatorial Indian Ocean in active phases of the Madden–Julian oscillation. *J. Atmos. Sci.*, **70**, 2713–2725, doi:10.1175/JAS-D-12-0311.1.